journal of the mechanical behavior of biomedical materials 160 (2024) 106719

Contents lists available at ScienceDirect

Journal of the Mechanical Behavior of Biomedical Materials

journal homepage: www.elsevier.com/locate/jmbbm

4D printing and optimization of biocompatible poly lactic acid/poly methyl methacrylate blends for enhanced shape memory and mechanical properties

Hossein Doostmohammadi [a], Kamyab Kashmarizad [a], Majid Baniassadi [a], Mahdi Bodaghi [b,*], Mostafa Baghani [a,**]

[a] School of Mechanical Engineering, College of Engineering, University of Tehran, Tehran, Iran
[b] Department of Engineering, School of Science and Technology, Nottingham Trent University, Nottingham NG11 8NS, UK

ARTICLE INFO

Keywords:
4D printing
Shape memory polymers
PLA/PMMA
Biocompatibility
Artificial neural network
Response surface methodology

ABSTRACT

This study introduces a novel approach to 4D printing of biocompatible Poly lactic acid (PLA)/poly methyl methacrylate (PMMA) blends using Artificial Neural Network (ANN) and Response Surface Methodology (RSM). The goal is to optimize PMMA content, nozzle temperature, raster angle, and printing speed to enhance shape memory properties and mechanical strength. The materials, PLA and PMMA, are melt-blended and 4D printed using a pellet-based 3D printer. Differential Scanning Calorimetry (DSC) and Dynamic Mechanical Thermal Analysis (DMTA) assess the thermal behavior and compatibility of the blends. The ANN model demonstrates superior prediction accuracy and generalization capability compared to the RSM model. Experimental results show a shape recovery ratio of 100% and an ultimate tensile strength of 65.2 MPa, significantly higher than pure PLA. A bio-screw, 4D printed with optimized parameters, demonstrates excellent mechanical properties and shape memory behavior, suitable for biomedical applications such as orthopaedics and dental implants. This research presents an innovative method for 4D printing PLA/PMMA blends, highlighting their potential in creating advanced, high-performance biocompatible materials for medical use.

1. Introduction

Smart materials represent a fascinating category, known for their ability to sense environmental conditions and to respond to external stimuli such as heat, pH changes, light, electromagnetic fields, humidity etc. (Fang et al., 2023; Niu et al., 2022; Chen et al., 2018; Gregor et al., 2017; Donate et al., 2020; Feng et al., 2022; Kiyani et al., 2021; Saeed et al., 2024). These materials are basically utilized in biomedical fields, electronic devices, sensors, actuators, artificial muscles and many other applications (Buckley et al., 2006; Hassan et al., 2018). Smart materials which are also known as advanced materials are broadly categorized into two types: passive smart materials and active smart materials (Hu and Bodaghi, 2023). Passive smart structures are a type of smart materials that respond to external stimuli without requiring control system. Instead, their responses are inherently built into their structure or composition like optical fibers. On the other hand, there are active smart materials which can transform one form of energy into another (e.g. piezoelectric materials by producing electric charge out of directional strain) or their properties remain unchanged when placed in an external stimulus (like photochromatic glass exposed to sunlight) (Ni et al., 2023; Subash and Kandasubramanian, 2020). Among smart materials, shape memory polymers (SMPs) have been extensively studied in the past two decades.

Thermosets are commonly known for their shape memory properties thanks to their crosslinking components (Li et al., 2018; Mora et al., 2019). However, thermoplastics can also demonstrate significant shape memory effects, particularly when they possess crystallinity or when they are blended with another polymer. In thermoplastic blends, the two-phase morphology contributes to the material's shape memory properties (Luo et al., 2024; Xia et al., 2021; Dayyoub et al., 2022). The rigid amorphous regions within these blends act similarly to the hard segments found in thermosets. When chemical crosslinking is not practicable, the entanglement and bonding between different polymer chains can mimic the effects of crosslinking, known as physical

* Corresponding author.
** Corresponding author.
E-mail addresses: mahdi.bodaghi@ntu.ac.uk (M. Bodaghi), baghani@ut.ac.ir (M. Baghani).

https://doi.org/10.1016/j.jmbbm.2024.106719
Received 9 July 2024; Received in revised form 22 August 2024; Accepted 3 September 2024
Available online 4 September 2024

Table 1
Parameters used in ANN and RSM.

Parameters	Unit	Values
Bed Temperature	°C	40
Layer thickness	mm	0.2
Nozzle diameter	mm	0.6
Hydraulic Pressure	bar	1

crosslinking (Lalegani et al., 2023; Nugroho et al., 2021). Furthermore, the advantages of thermoplastics, including ease of manufacturing, low cost, and recyclability, make them favorable alternatives to thermosets. Biodegradable thermoplastics have gained worldwide attention due to their sustainability and the role in reducing plastic pollution.

Poly lactic acid (PLA) is an aliphatic biodegradable polyester which is extensively employed in 3D printing owing to its excellent processability and its mechanical robustness. Despite its advantages, PLA possesses low heat distortion, poor impact strength, and limited shape recovery. To address these weaknesses and broaden its potential applications, researchers have explored blending PLA with other thermoplastics (Tancogne-Dejean et al., 2018; da Cunha et al., 2023; Zhang et al., 2021; Gaxiola-Ló et al., 2022; Rodrigues et al., 2016; Anakabe et al., 2018). Among them, poly methyl methacrylate (PMMA) stands out as a promising candidate for melt-blending with PLA, owing to the high degree of chain entanglement that can be formed between them along with its good impact resistance, perfect thermal stability, mechanical strength and more importantly its biocompatibility (Pathak et al., 1998; Shi et al., 2023; Samal et al., 2023).

Recent rapid advancements in additive manufacturing techniques have significantly changed the production landscape which allows fabrication of a diverse structures across various scales for a multitude of industries and applications (Spiegel et al., 2022; Alshebly et al., 2021; Gastaldi et al., 2023; Zhao et al., 2023). The utility of 3D printing extends across a wide range of applications including biomedical implants, bone scaffolds, soft tissues, prototyping, mass production, automotive applications and more (Moradi et al., 2023; Asvar et al., 2017). Within the domain of smart materials, additive manufacturing, particularly 3D printing, plays a crucial role, often termed as 4D printing (Sondagar et al., 2024; Raja et al., 2024). The designation '4D' denotes the capacity of 3D printed objects to change one of their properties in response to external stimuli (Raja et al., 2024). Fused deposition modelling (FDM) is the most common 3D printing technique used to fabricate thermoplastic printed parts (Naresh et al., 2024). In this technique, the feed for fabricating parts is a continuous filament which is produced by an extruder. Accessibility and ease of use are the pros of FDM (Shanmugam et al., 2024). Nevertheless, it only works with filaments and does not have material variety. On the other hand, pellet-based 3D printers are a new additive manufacturing technique that can be employed for a wide range of materials (Zhang and Luo, 2024). This includes not only thermoplastics like Acrylonitrile Butadiene Styrene (ABS) and PLA but also, it's possible to blend different materials directly in the printer which allows the creation of custom material formulations tailored to specific applications. It is also applicable for composites with fillers and nano/micron particles. Besides, using pellets directly can reduce waste in the printing process since there's no need for filament spools, which can generate excess material that is often discarded.

As many parameters contribute to physical and mechanical

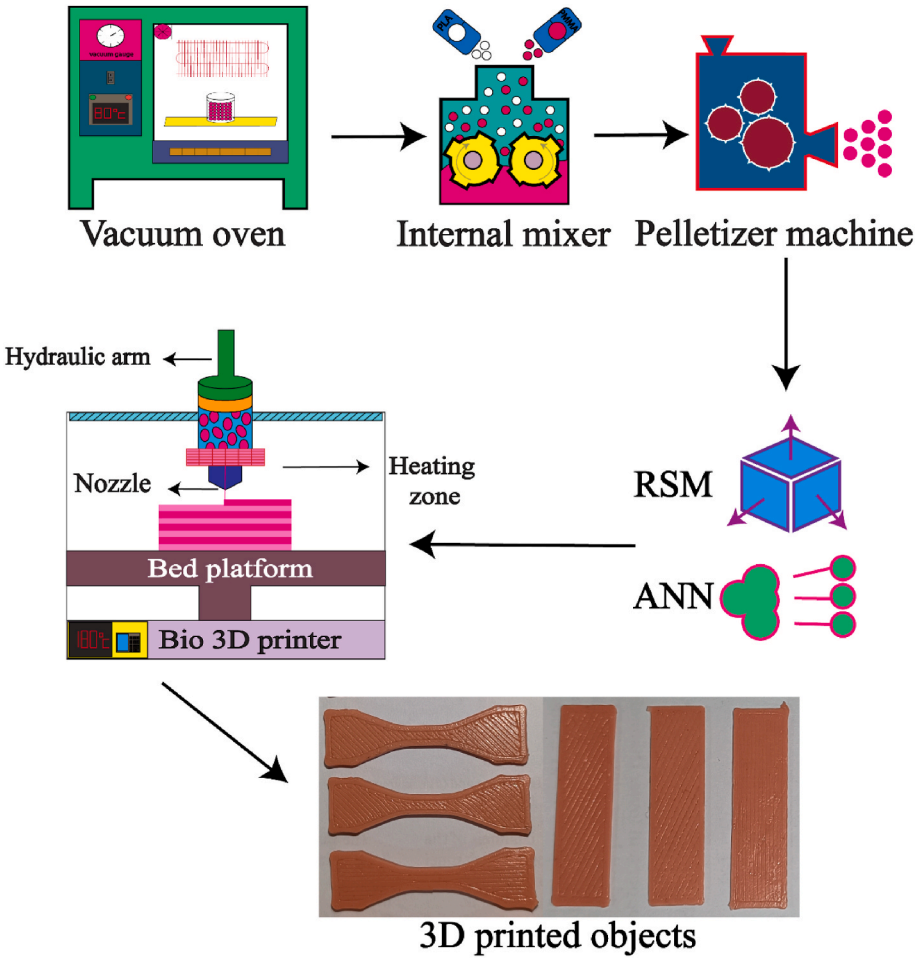

Fig. 1. Schematic of material processing and 3D printing.

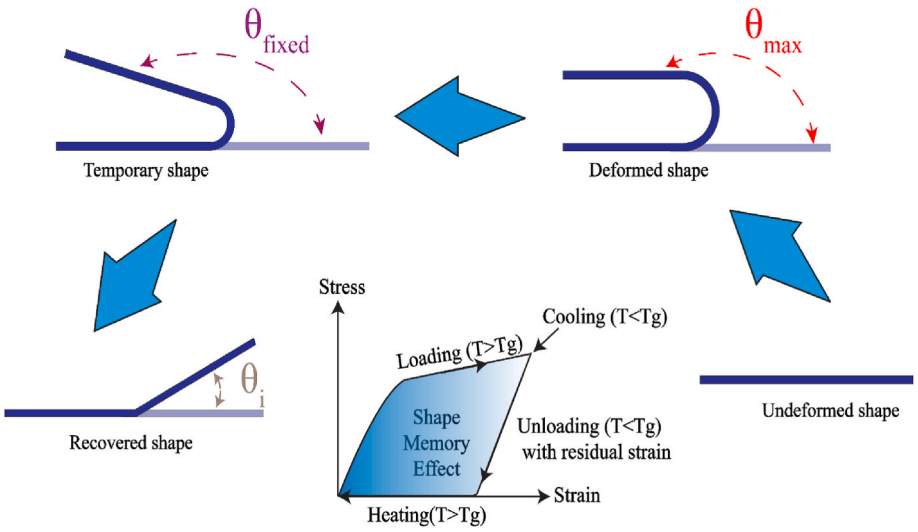

Fig. 2. Schematics of shape memory programming and activation steps.

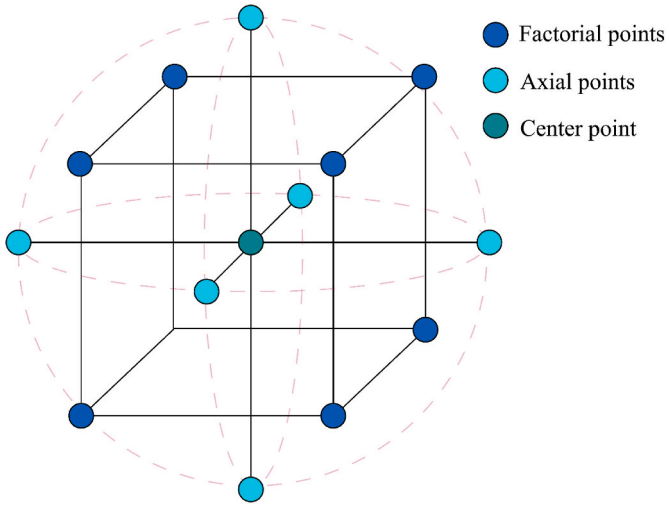

Fig. 3. Schematics of central composite design.

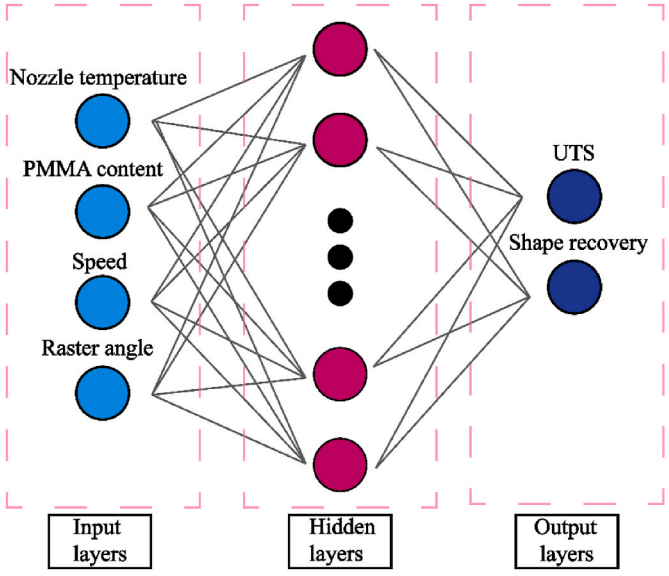

Fig. 4. Schematics of ANN

Table 2
Design variables and levels in RSM.

Parameters	Unit	Low level (−1)	Center (0)	High level (+1)
Nozzle Temperature	°C	180	190	200
PMMA content	%	40	50	60
Printing speed	mm/min	300	500	700
Raster angle	–	0/90	30/-30	45/-45

properties of the blends, response surface methodology (RSM) and artificial neural network (ANN) have been utilized in many research studies to predict the optimized parameters for having the most desired outputs (Das et al., 2023; Shirzad et al., 2021). There are several successful examples of utilizing ANN and RSM in predicting the optimized 3D printing parameters for desired outputs. Domingo et al. studied the effect of 3D printing parameters like nozzle diameter, velocity and layer thickness on the fatigue behavior of ABS specimens utilizing design of experiment (DOE) (Domingo-et al., 2018). Their results proved that infill density is the main parameter that affects the fatigue behavior of the honeycomb and rectilinear architectures. Zolfaghari et al. (Zolfagharian et al., 2023) employed RSM to investigate the effect of different printing parameters on designing bi-stable soft robotic grippers. The optimized parameters helped fabrication grippers with fast bending which is highly desired in robotics. Yadav et al. (2020) worked on optimizing infill density, extrusion temperature and material density for having the best ultimate tensile strength (UTS) in ABS and Polyethylene Terephthalate Glycol (PETG) utilizing ANN and genetic algorithm-artificial neural network (GA-ANN). Their studied showed that GA-ANN can enhance mechanical strength by 4.59%.

In earlier research, it was observed that a 50/50 wt ratio blend of PLA and PMMA results in a partially co-continuous morphology, leading to excellent shape memory properties and strong mechanical performance. To investigate the shape memory effects of PLA/PMMA blends with varying weight ratios, Samuel et al. (2014) conducted dual shape memory tests. They found that for the symmetric blend (50/50 wt of PLA/PMMA), the switch temperature (the temperature at which the material transitions from its temporary shape back to its original shape) increased from 70 °C to 90 °C, while the stretching temperature rose from 65 °C to 94 °C. This blend demonstrated a high shape fixity ratio of 99% and a shape recovery ratio of 90%. In contrast, asymmetric blends

Table 3
ANN architecture.

Training algorithms	Input layer	Hidden layers		Output layers	
	Number of neurons	Number of neurons	Activation function	Number of neurons	Activation function
Bayesian Regularization Back Propagation	4	4	SELU	2	Purelin (linear)

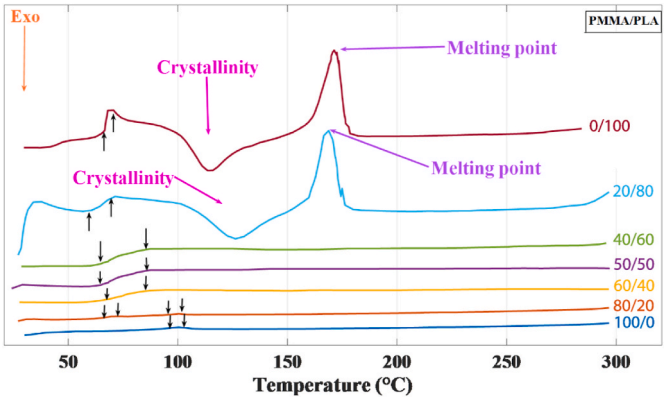

Fig. 5. DSC results of PLA/PMMA samples.

Table 4
Glass transition temperature (T_g), its broadness (ΔT_g) and crystallinity (X_c) of PMMA/PLA blends.

PLA/PMMA	T_g (°C)	ΔT_g (°C)	X_c (%)
100/0	67	12	13.4
80/20	65	17	11.9
60/40	69	34	0
50/50	72	40	0
40/60	74	35	0
20/80	64/98	10/12	0
0/100	104	15	0

with 30% and 80% PMMA showed shape recovery ratios below 80%. Additionally, triple shape memory tests were performed, fixing temporary shapes at 94 °C and 65 °C. All symmetric samples recorded a shape recovery of 60% for the first shape and over 90% for the second shape.

Previous studies have not 4D printed PLA/PMMA blends due to fundamental challenges. PMMA's high melting point complicates uniform extrusion, and its tendency to shrink upon cooling leads to warping and distortion of printed parts. These issues limit the utilization of these materials in biomedical applications, which require the creation of complex architectures achievable only through advanced 3D printing technologies.

To overcome these challenges, this study employs a novel approach using a custom-made pellet-based bio-3D printer, effectively bypassing the difficulties associated with filament fabrication. By utilizing ANN and RSM, this research optimizes key parameters to maximize the UTS and shape recovery ratio of PLA/PMMA blends. The materials used include Poly L-lactic acid (PLLA) filament and PMMA granules, which are melt-blended and processed into pellets for 3D printing. Differential Scanning Calorimetry (DSC) tests are conducted to analyse the thermal transition temperatures and broadness of the blends which identifies those with the highest compatibility based on broad thermal transition regions. The input parameters for the RSM and ANN models include nozzle temperature, printing speed, raster angle, and PMMA content in the polymer matrix, particularly focusing on blends with broad glass transition temperature regions. This comprehensive approach aims to 4D print PLA/PMMA composite bio-screws with enhanced mechanical properties and shape memory capabilities, suitable for advanced biomedical applications such as orthopaedics and dental implants.

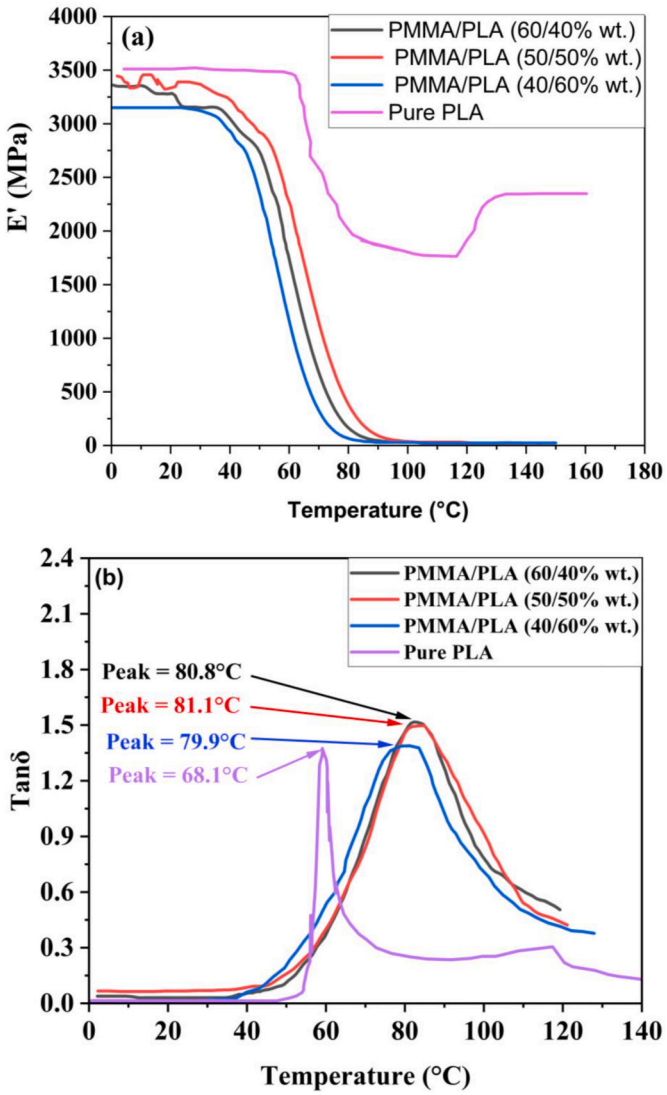

Fig. 6. (a) Storage modulus and (b) tanδ of pure PLA and PLA/PMMA blends.

2. Materials and methods

2.1. Materials

Poly L-lactic acid (i.e., PLLA) filament ($\rho = 1.23$ g/cm^3, melt flow rate = 6 g/10min) and poly methyl methacrylate (PMMA) granules ($\rho = 1.19$ g/cm^3, melt flow rate = 3.8 g/10min) were supplied by YOUSU 3D technology Co. and CHIMEI Co. respectively.

2.2. Processing and 3D printing

PLA filaments were chopped into small pieces utilizing a pelletizer machine, then along with PMMA granules were placed in a vacuum oven at 85 °C overnight to remove any moisture. The materials were then added to an internal mixer (Baopin Technology co.) and were melt-

Table 5
ANOVA table with terms of each variable and the interconnected terms for model prediction- *NU denotes the term which is not involved in the model.

	UTS	Shape recovery
Source	P	P
Model	0.0002	0.0089
A- Temperature	0.4157	0.7603
B- Raster angle	0.0308	0.0061
C- Speed	0.3030	0.3558
D- PMMA content	0.0713	0.5260
AB	0.9155	***NU**
AC	0.9359	***NU**
AD	0.4956	0.6675
BC	0.7734	0.0810
BD	0.0095	***NU**
CD	0.0302	0.1401
A^2	0.1932	0.0460
B^2	0.0008	0.0020
C^2	0.5315	0.0023
D^2	0.7622	***NU**
Anticipated R^2	0.9276	0.88
lack of fit	0.3423	0.5935

Table 6
The optimal ANN parameters for predicting UTS and shape recovery ratio of the composites.

MLPS	Learning rate	Momentum	Training RMSE	Cross validation RMSE	Epochs
4-12-6-2	0.62	0.43	0.036	0.041	18000

Table 7
Comparison of predicted vs. actual values in ANN and RSM.

	Shape recovery		UTS	
Parameters	ANN	RSM	ANN	RSM
MAE	1.64	3.0657	1.3334	2.1918
R^2	0.9536	0.8588	0.9615	0.9145
RMSE	1.8002	3.2525	2.1918	2.6916

blended for 18 min at 180 °C with twin screw speed of 70 rpm. The blends were then compressed by compression-moulding technique to form sheets. The obtained sheets were then placed in a bath of liquid nitrogen right after the compression-moulding step to prevent crystallization of PLA. PLA has low crystallinity and its crystallites do not allow full interaction between PMMA and PLA chains. Next, sheets were chopped into pellets to be added in pellet-based bio-3D printer. The pellet-based 3D printer has a cylindrical chamber that exhibits a heater at its bottom. The material melts in the chamber and a hydraulic arm forces the material through the nozzle. The 3D printing constants are presented in Table 1 and the whole process is schematically presented in Fig. 1.

2.3. Characterization

To study the thermal behavior and the compatibility of the materials, DSC based on ASTM D3418-21was utilized. DMA Q850 was utilized to study the physical properties of the polymer blends and field emission scanning electron microscopy (FE-SEM) analysis were carried out utilizing DSC 214 Polyma and TESCAN Mira 3 respectively. DSC was performed under heating range of 25–300 °C with heating rate of 20 °C/min. The crystallinity of the samples were then calculated according to Eq. (1). Gold coated (10 nm thickness) samples with dimension of 10 × 10 × 1 (mm^3) were employed for FE-SEM analysis.

For evaluating shape memory properties, samples of 30 × 10 × 1 (mm^3) were 3D printed. As shown in Fig. 2, assessing shape memory properties contain two steps of programming and activation. In programming step, samples were bent into "U shapes" (temporary shape) at 100 °C (nearly 25 °C higher than glass transition temperature of the blends). Next, the samples were cooled to room temperature and then the force was removed. The activation step began with heating up the samples to 100 °C. At this temperature, the samples recover their original shape (permanent shape). The shape memory properties of the samples were assessed in this study using the following equations (Eqs.) to determine the shape recovery ratio (R_r) and shape fixity ratio (R_f)

$$X_c = \frac{\Delta H_m}{\Delta H_m^0 (1-\phi)} \times 100\% \quad (1)$$

$$R_f = \frac{\theta_{fixed}}{\theta_{\max}} \times 100\% \quad (2)$$

$$R_r = \frac{\theta_{\max} - \theta_i}{\theta_{\max}} \times 100\% \quad (3)$$

In equation (1), ΔH_m is the heat of melting obtained from the area under the melting peak, ΔH_m^o is the heat of melting for a 100% crystalline sample of the same polymer, which can be found in standard reference tables. The heat of melting for 100% crystalline poly (L-lactic acid) (PLA) is approximately 93.7 J/g (Ertiletskaya et al., 2023). and φ is the volume fraction of the polymer phase and in equations (2) and (3), θ_{max} represents the target angle for shape retention, θ_{fixed} is the angle that remains after the constraints are removed, and θ_i is the unrecovered angle. A schematic of shape memory tests is presented in Fig. 2.

For tensile tests, samples were 3D printed according to ASTM-D638 (type-V). Nevertheless, the clamping length was reduced due to restriction in gripper of universal testing machine (SANTAM-STM05). The tests were done with the stretching rate of 1(mm/min).

2.4. Response surface methodology

Response surface methodology was utilized to predict the optimum 3D printing parameters and PMMA content for shape recovery process and UTS. In this respect two central composite experimental designs (CCD) with 4 independent variables were employed. This design is characterized by its ability to explore both linear and quadratic effects, as well as interactions between different factors in a systematic way. Central composite design typically consists of a factorial portion, a set of center points, and a set of axial points that are located at various distances from the center (Fig. 3). The CCDs were performed by Design Expert v.13.0.1with 26 runs and α = 1. Each run represents two samples (One for shape memory and one for tensile test, each with the aforementioned size). Table 2 displays the variables and levels. The correlation between the variables and the responses were calculated by second-order polynomial Eqs. as given below:

$$Y = \beta_0 + \sum_{i=0}^{n} \beta_i X_i + \sum_{i=0}^{n} \beta_{ii} X_i X_i + \sum_{i=0}^{n-1} \sum_{j=i+1}^{n} \beta_{ij} X_i X_j + \varepsilon \quad (4)$$

where β_0, β_i and β_{ii} are constant, linear coefficient and squared coefficient, β_{ij} is the cross-product coefficient, n is the number of factors (n = 4), X_i is the real value of the independent variable and ε is the error term which is typically assumed to be normally distributed with a mean of zero.

2.5. Artificial neural network methodology

The Artificial Neural Network (ANN) is a mathematical model inspired by the structure and functioning of the human brain and nervous system. ANNs work by simulating the behavior of interconnected neurons in the human brain to process complex information and make predictions or classifications (Zolfagharian et al., 2021). In the current

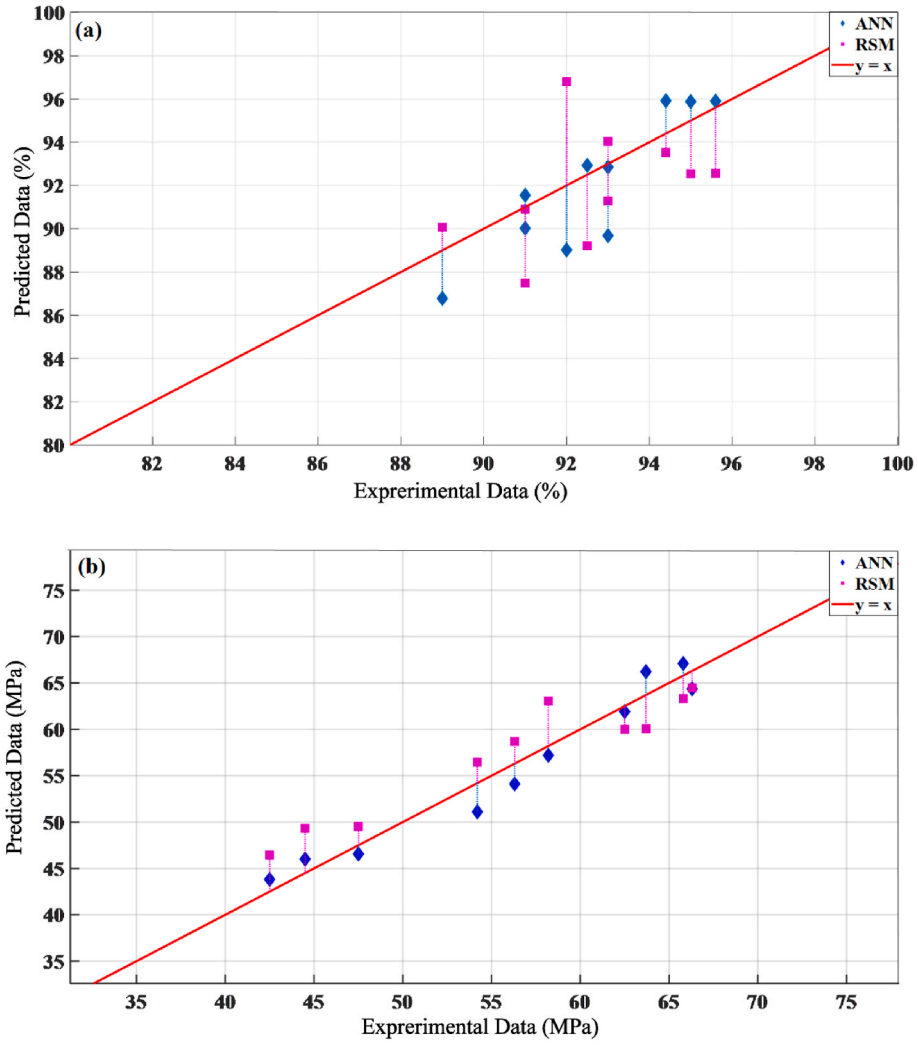

Fig. 7. Experimental and predicted values for (a) shape recovery ratio and (b) UTS.

study ANNs have been applied on the same data used for RSM. As depicted in Fig. 4, ANN has some inputs, hidden layers and outputs. Between the input and output layers, there may be one or more hidden layers. These layers contain neurons that process the input data through weighted connections and activation functions. These layers consist of neurons that transfer weights by functions. The transfer functions used in this work are given as below:

$$F(x)=\lambda\begin{cases} x, if\ \ x>0 \\ \alpha e^{x}-\alpha, if\ \ x\le 0 \end{cases} \quad -\infty \le F_i \le +\infty \tag{5}$$

$$F_i = x \quad -\infty \le F_i \le +\infty \tag{6}$$

After testing various training functions, it was discovered that the Bayesian regularization (BR) algorithm yields the best results with minimal square root error since it incorporates Bayesian principles to prevent overfitting, which is especially beneficial for small data sets where overfitting is a common issue, also it can adapt well to varying data distributions and complexities which is again an advantage for small data sets with diverse characteristics. The ANN architecture used for this work is presented in Table 3., it should be noted that the ANN used 21 random data for training and checked the results with the other five for reaching the best performance. The model uses Scaled exponential linear unit (SELU) activation function due to its better performance than rectified linear unit (ReLU) activation functions for this problem.

2.6. Error functions

In this work, three error functions were used to validate the performance of ANN and RSM.

$$R^2 = 1 - \frac{\sum_{m=1}^{n}\left(Y_{m,e}-Y_{m,p}\right)^2}{\sum_{m=1}^{n}\left(Y_{m,p}-Y_{e}\right)^2} \tag{7}$$

$$RMSE = \sqrt{\frac{\sum_{m=1}^{n}\left(Y_{m,p}-Y_{m,e}\right)^2}{n}} \tag{8}$$

$$MAE = \frac{1}{n}\sum_{m=1}^{n}\left|Y_{m,e}-Y_{m,p}\right| \tag{9}$$

where R^2 is the coefficient of determination and RMSE is the root mean square error, $Y_{m,e}$ and $Y_{m,p}$ are the experimental and predicted values respectively. n represents the number of experiments and Y_e represents mean square value of experimental data.

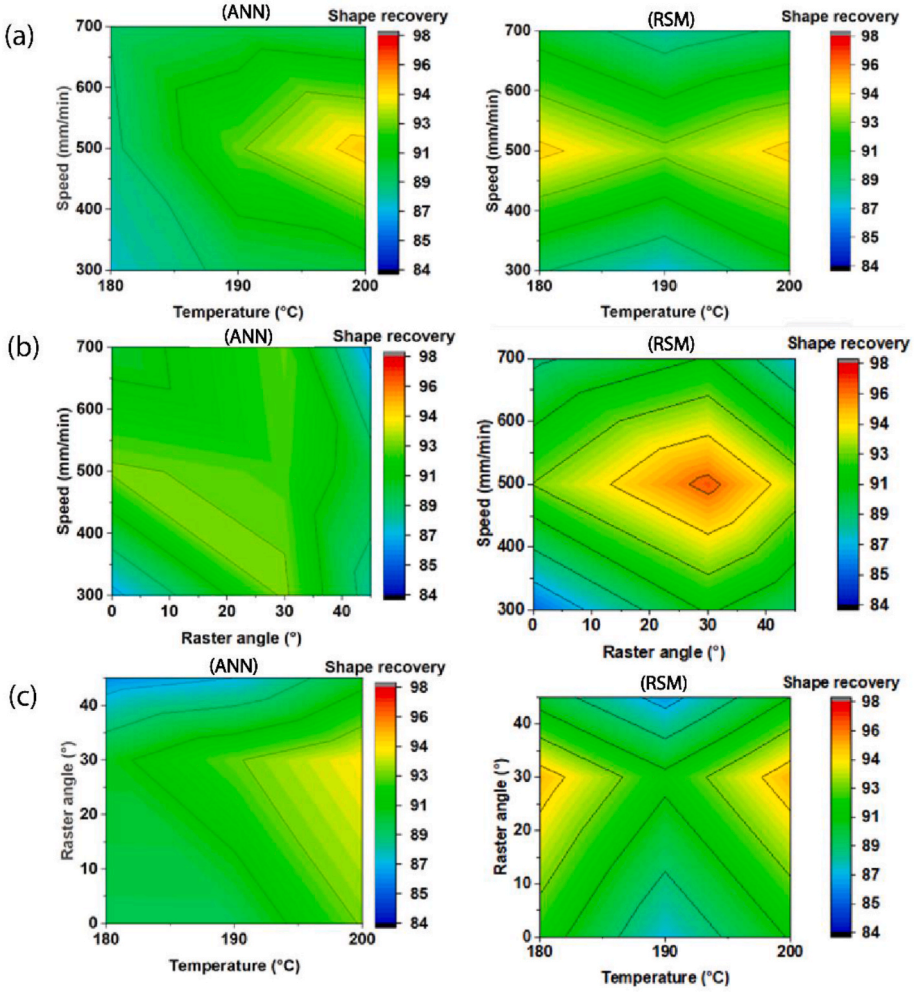

Fig. 8. the effect of model parameters on shape recovery ratio of PLA/PMMA blends.

3. Results and discussion

3.1. Differential Scanning Calorimetry

The miscibility, thermomechanical behavior and crystallinity of polymer blends have been investigated by DSC and DMTA. According to Fig. 5, the two consequent black arrows show the glass transition region of each polymer blends. In pure PLA, the glass transition region is between 60 °C and 72 °C. the crystallites start to form at 103 °C. and the melting point was recorded at 171 °C. the same trend was observed for PMMA/PLA with 20/80 %wt. which indicates that PMMA phase did not influence the crystallinity of PLA. For 80/20 and 0/100 %wt. of PMMA/PLA blends two glass transition regions can be noticed which means that there are not compatible. High compatibilities with broad thermal transition regions are observed in polymers with PMMA content of 40 % wt., 50 %wt. and 60% wt. This region is as broad as around 35 °C for all three compatible blends. Broad thermal transition regions allow multiple shape memory effect, additionally, it brings more flexibility in tuning the activation temperature for shape memory behavior which makes it suitable for different applications. Hence, these three blends were chosen as one of the four parameters used for RSM and ANN inputs. It can also be noticed that in these samples PLA and PMMA chains could make fully dispersed interconnections. This can be confirmed by having no sign of crystallinity in the curves. More details about crystallinity are provided in Table 4. DMTA results in Fig. 6 also confirm the results of DSC. Broad thermal transitions seen in Fig. 6 (a) and 6 (b) for PLA PMMA blends with 40/60%, 50/50% and 60/40% are almost the same. The peaks of tanδ and its broadness indicate long α-relaxation time compared to pure PLA. The broad tanδ also indicates that two thermal transition temperatures overlap and one single peak is observed. This shows that different segments of both polymers relax within a long α-relaxation time and it takes time for each chain of one phase to be released from the other. This broadness confirms that a good portion of PLA and PMMA chains are fully entangled and this entanglement plays part in shape memory mechanism which is discussed in the shape memory test section.

3.2. Artificial neural network and response surface methodology

3.2.1. RSM

To show the significance of each coefficient in RSM modelling, an analysis of variance was conducted which is needed to determine the pattern of mutual interactions between each individual variable. The terms are called significant if the values of P are less than 0.05. Additionally, model terms with $P > 0.1$ are not significant. Some quadratic and linear terms are omitted in the analysis as it results in better model fit for shape recovery. Table 5 demonstrates the significance of each variable on shape recovery percentage and UTS. According to the table, terms B, BD, CD and B^2 in UTS and terms B, A^2, B^2 and C^2 in shape recovery are significant. Hence, the raster angle plays a crucial role in both models and quadratic terms of temperature and raster angle are significant. The lack of fit in both models are not significant which means that our model fits properly. R^2 value of shape recovery is around 0.8 which was predictable due to the close value ranges.

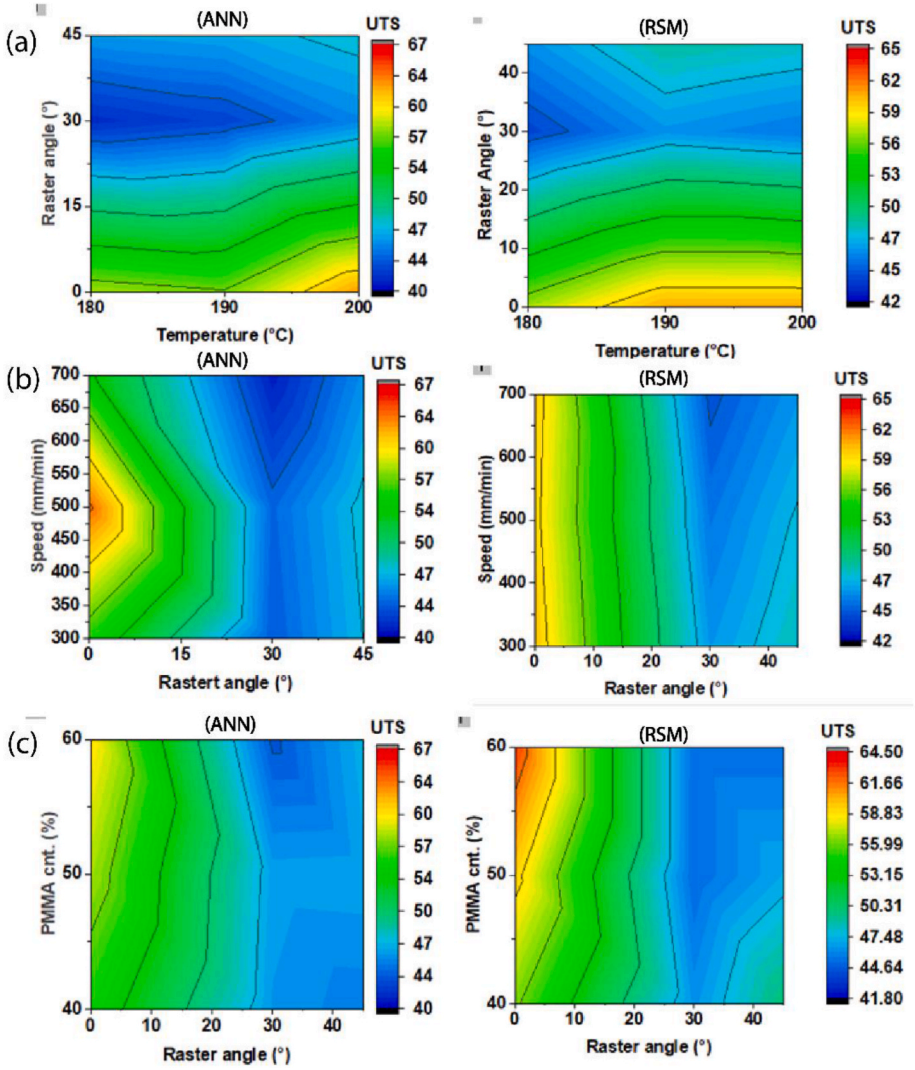

Fig. 9. the effect of model parameters on UTS of PLA/PMMA blends.

3.2.2. ANN

Multi-layer perceptron structure (MLPS) represents a fundamental type of ANN that has a hierarchical structure and is comprised of an input layer, one or more hidden layers, and an output layer. The defining characteristic of MLPs lies in the fully interconnected nature of their layers, where each neuron in a given layer is linked to every neuron in the subsequent layer via weighted connections. During training, MLPS uses a process called backpropagation to adjust the weights of these connections which minimizes the error between predicted and actual outputs. In the developed ANN model, the most suitable MLPS was selected as 4-12-6-2. The optimal configuration of the ANN parameters, including momentum, epochs, and learning rate were determined for the MLPS proposed in this study. The RMSE for the validation data set was determined so that the optimal number of epochs can be identified. Epochs were limited to 18000 for avoiding overfitting. The momentum was selected by choosing a reasonable range and then the best value was selected. The selected parameter values, which yielded the highest predictive performance for the output variables, are provided in Table 6.

3.2.3. Comparison of RSM and ANN

The ANN and RSM models were compared for their predictive capabilities. As mentioned in the paper, MAE, RMSE and R^2 are the parameters used for this comparison. Table 7 shows the computed values for these parameters and Fig. 7 indicates the resemblance of the predicted value vs. actual values for UTS and shape recovery ratio of the composite samples. The ANN model displays excellent accuracy in both outputs. Unlike the UTS results, the RSM model does not show high accurate results for shape recovery ratio. This can be reasonable since the values of shape recovery ratio are within a close range. In general, the RSM model shows higher deviation in comparison with the ANN model. In this work ANN performance was more significant that the RSM as ANN has higher capacity in generalization and is more capable in approximating the nonlinear systems whereas RMS model is limited to a specific polynomial form. Another limitation of RSM models is the optimization of multiple responses, which can be accomplished more easily in the ANN model. To achieve reasonable accuracy with the RSM model in multi-responses tasks, it is necessary to run it multiple times. Therefore, the ANN model is favored over the RSM model in terms of its generalization capability, approximation of nonlinear systems, and handling of multiple responses.

3.3. 3D and 4D printing based on RMS and ANN results

The 3D printing parameters and PMMA content were analyzed for both tensile and shape memory tests in Figs. 8 and 9 respectively. Only three significant contours for each are shown here, with the rest available in the supplementary material. All parameters are shown to be vital in determining optimal results. The RSM model indicates that a raster

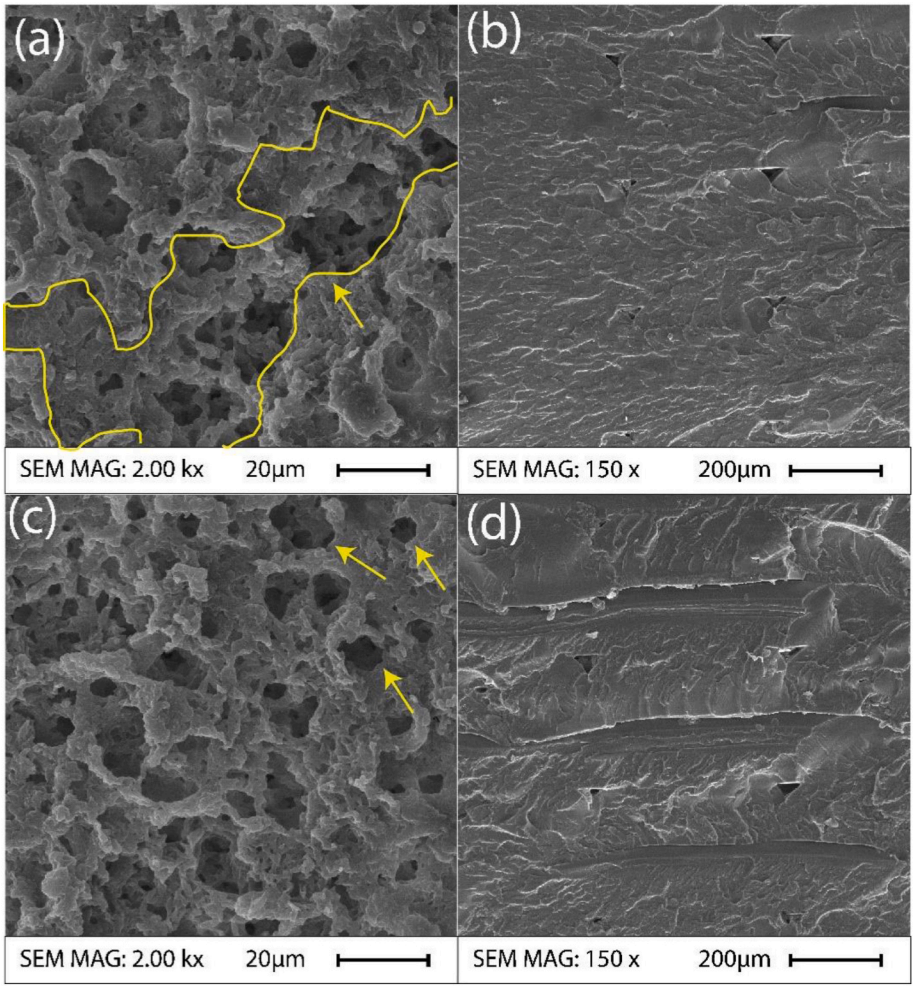

Fig. 10. SEM of Etched samples and cross sections of PLA/PMMA with (a, b) 50/50% wt. and (c, d) 40/60% wt. respectively.

angle of 30°/-30° (represented by 30° in contour plots) yields the best shape recovery ratio, as indicated by the maximum values surrounding it. The ANN model however, is more complex than RSM and presents challenges in discussing the results of raster angle. The same complexity applies to the speed parameter. A moderate printing speed ensures uniform material flow, while temperature also plays a crucial role in achieving uniform 3D printing. Higher temperatures are more suitable for shape memory tests, evidenced by both ANN and RSM models in all contour plots. Therefore, higher temperatures result in more uniform printing of specimens in this case. In Fig. 9, the influence of PMMA content is more obvious. Higher content of PMMA resulted in higher ultimate stresses. It is possible that the expected uniform core-shell morphology led to that. Polymer core-shell morphology which in many research studies is referred to as sea-island morphology is a type of morphology seen in polymer blends. Sea-island morphology is a specific type of phase-separated structure commonly observed in polymer blends. In this arrangement, one phase (the "sea") is continuous, while the other phase (the "island") is dispersed within it as discrete domains. The islands are usually small and can vary in size and shape depending on the processing conditions and the compatibility of the two phases. The well distribution of islands within the sea phase can significantly enhance the material's overall performance. Raster angle with 0°/90° (represented by 0° in contour plots) is supposed to have the best impact on tensile strength. Speed and temperature behaviors is almost different in each model and is complex to be discussed.

4. FE-SEM

The results from the ANN and RSM analysis revealed that materials containing 50% and 60% PMMA content exhibited the highest performance in shape memory and tensile tests, respectively. Figs. 10 (a) and Fig. 10 (c) show the morphology of etched samples for PLA/PMMA blends with 50/50% wt. and 40/60% wt., respectively. Fig. 10 (b) and Fig. 10 (d) display the cross sections of the samples in the same order. In Fig. 10 (a), a partial co-continuous morphology is evident, while fully dispersed PLLA droplets are observed in Fig. 10 (c). These different morphologies impact the shape memory properties, as discussed in detail in the shape memory test section. The fully dispersed sea-island morphology in Fig. 10 (c) enhances stress distribution, while the cross section of both materials shows high printing quality without defects, leading to improved shape fixity, recovery, and load distribution. Furthermore, materials with minimal defects exhibit consistent shape memory cycles with minimal changes in shape fixity and shape ratio.

5. Tensile test

According to the predictions of both models and experimental test that were conducted (All predictions are provided in the supplementary file), the best tensile test specimen was 3D printed with 60% of PMMA content, raster angle of 0°/90°, printing speed of 500 mm/min and temperature of 200 °C. The strength of the specimen was 65.2 MPa which is around 3% more than the predicted value by ANN (68.7) and 5% compared to RSM guess (61.23). Fig. 11 (a) illustrates the specimen

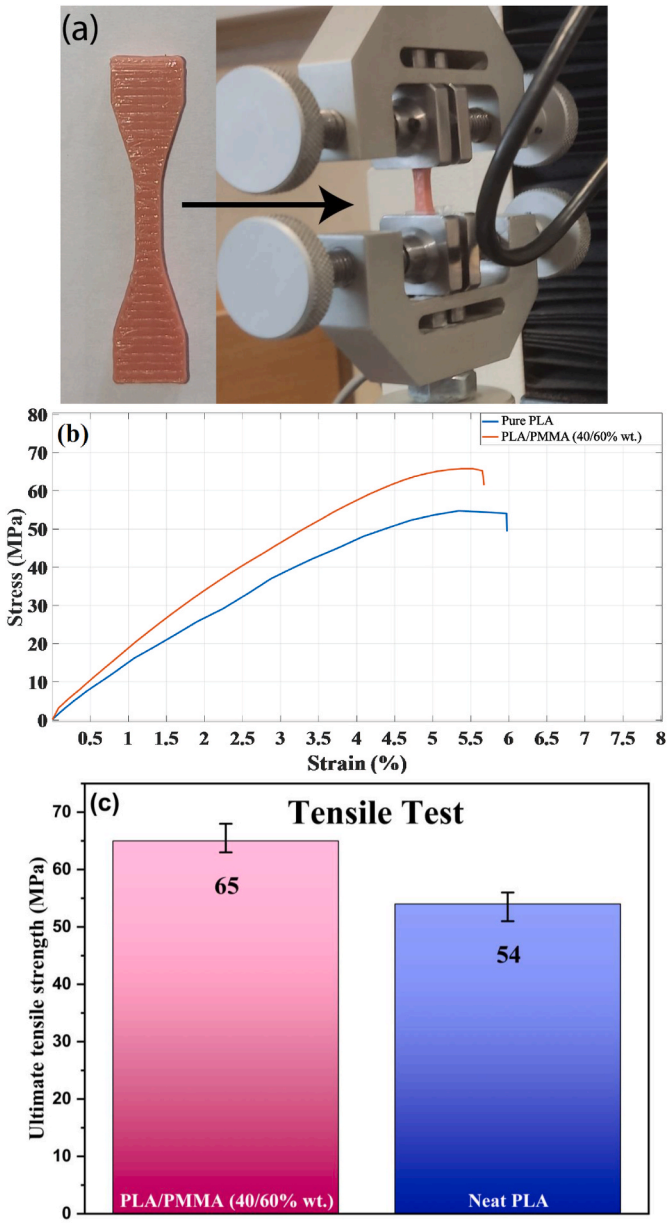

Fig. 11. (a) Tensile test specimen and testing machine (b) tensile test plot and (c) the UTS of the materials.

and the tensile test. The results are presented in Fig. 11 (b). As it is displayed, addition of PMMA with equal weight portion to PLA caused an increase in ultimate tensile strength of the material. As demonstrated in the previous section (FE-SEM) Also, the strain at break was recorded the same for both material which indicates that addition of PMMA does not influence its elongation. All in all, it is to believe that the material is mechanically robust and can be used in applications like bio-screws for bone fractures and bio-robotics due to its biocompatibility.

6. Shape memory test

The research study done by Shi et al. (2013) provided information about the complex behavior of blends with broad glass transitions which reveals that the presence of multiple individual glass transitions corresponds to different shape memory elements within nano-domains. This indicates that during the shape recovery process, the high T_g and low T_g nano-domains containing varying amounts of oriented PLA/PMMA can be selectively activated. The researchers identified three distinct mechanisms at play when the composites were subjected to direct heating stimulator. At lower switch temperatures (around 60 °C–75 °C), the soft domains formed by PLA rich nanodomains drive shape changes primarily through the action of PLA chains. Moving into the temperature range of 75 °C–85 °C, shape changes are enabled by the presence of highly entangled PLA and PMMA chains. At higher switch temperatures approaching 90 °C, only the PMMA chains within the PMMA rich domains are thermally activated. In light of these findings, a stretching temperature of 100 °C was selected to ensure that all chains are actively involved in the shape changing process. This careful consideration of temperature parameters highlights the intricate interplay between different chain configurations and their roles in shape memory behavior within the nanocomposite material. The full process is depicted in Fig. 12 (a). According to the results, the best shape memory specimen has 50% of PMMA content, with 3D printing speed of 190 °C, speed of 300 mm/min and raster angle of 30°/-30°. Two types of tests were performed. The first test was carried out in hot water in bending mode and the second one was performed in stretching mode in DMA Q850 from TA instrument. The sample showed perfect shape fixity in both tests (100%). The results for the test in hot water is provided in Fig. 11 (b) which shows an excellent shape recovery ratio (100%) within 5 s (Movie S1). This result was predicted with 5% error in ANN and 6% error in RSM models. The shape recovery ratio in tensile mode is calculated differently from the bending mode as it can be computed according to Eq. (4). The shape recovery was recorded 97.8% which shows the effect of timing while both displayed maximum shape fixity ratio (Fig. 12 (c)). The effect of time played a role in the observed differences in shape recovery ratio between the two testing modes. In the tensile mode with higher time, the material has been exposed to prolonged stress and strain, which could potentially lead to some level of permanent deformation or memory loss in the material. This could affect its ability to fully recover its original shape compared to the bending mode with a shorter duration of testing.

Supplementary video related to this article can be found at https://doi.org/10.1016/j.jmbbm.2024.106719

7. Potential applications

As previously discussed, both PLA and PMMA are known for their biocompatibility, a characteristic that is also present in PLA/PMMA blends. Moreover, these blends exhibit superior UTS and shape memory properties compared to pure PLA, which is commonly used for bio-scaffolds and implants. Utilizing the optimal 3D printing parameters identified through RSM and ANN models, a bio-screw and a bio-scaffold were successfully 3D printed for maximum UTS (Fig. 13). This 3D printed parts can be effectively used to address bone defects in orthopedic procedures and the bio-screw can serve as dental implants due to its mechanical robustness, full biocompatibility, and high stability. Additionally, the blend's shape memory properties are advantageous for such applications. It should be noted that the bio-parts temporary shape can be fixed in a within a temperature range of 60 °C–70 °C, where PLA chains act as soft domains since the material has a single broad thermal transition temperature and therefore the bone cells do not suffer considerable damage. It should be mentioned that a temperature of 70 °C can be harmful when it directly affects the bone tissues. However, in this case, the temporary shape of the SMPs has no direct interaction with bone tissue (As depicted in Fig. 13). Instead, localized heat is applied to the specimen itself—not the bone. Due to its rapid recovery, the entire process completes in less than 6 s and consequently, this process is not harmful to the bone tissue.

8. Conclusion

In this research, PLA/PMMA blends were successfully 4D printed for the first time. The study utilized ANN and RSM models to identify the optimal 3D printing parameters and PMMA content needed to achieve

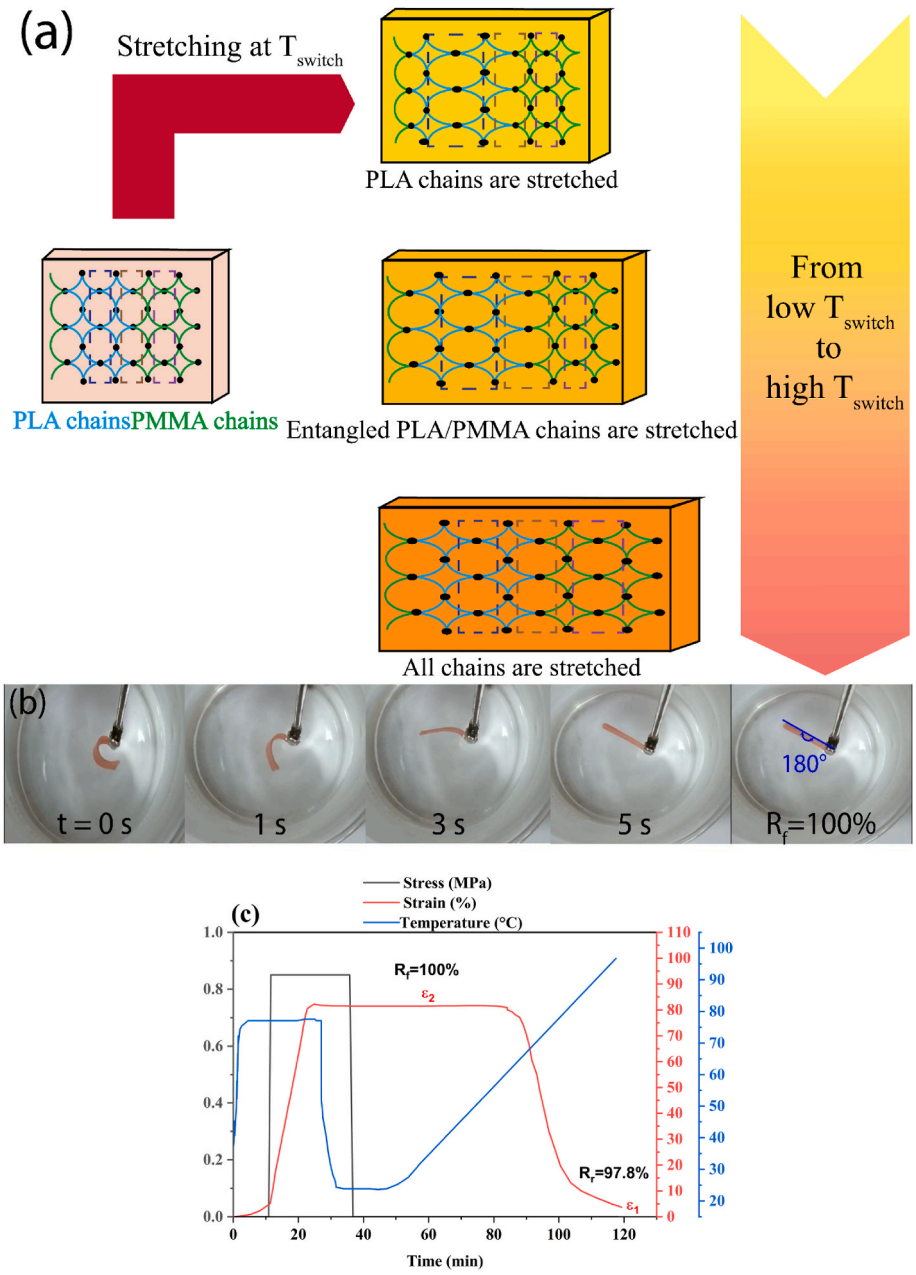

Fig. 12. (a) Shape changing mechanisms, (b) shape memory test in bending mode and (c) in tensile mode.

the desired shape recovery ratio and ultimate tensile strength. Both models provided accurate predictions, with the ANN model demonstrating greater flexibility in handling nonlinear relationships compared to the RSM model. The predicted data closely matched the experimental results, as indicated by the error functions. The blends with a 50/50% weight ratio of PLA to PMMA exhibited the best shape memory performance, achieving a shape recovery ratio and shape fixity of 100%. Comparative shape memory tests in tensile and bending modes revealed that the time factor negatively impacted the shape recovery ratio. Additionally, the blend with a 40/60% weight ratio showed an ultimate tensile strength of 65.2 MPa, which is 17% higher than that of pure PLA. These findings suggest that PLA/PMMA blends, due to their high performance and biocompatibility, could serve as a suitable alternative to pure PLA in shape memory components and biomedical applications requiring mechanically robust polymers. To demonstrate this, a bio-screw and a bio-scaffold were 3D printed, showcasing excellent 3D printability and potential applications in biomedical fields such as orthopaedics and dental implants.

CRediT authorship contribution statement

Hossein Doostmohammadi: Writing – review & editing, Writing – original draft, Visualization, Software, Methodology, Investigation, Data curation, Conceptualization. **Kamyab Kashmarizad:** Writing – review & editing, Visualization, Software, Methodology, Investigation, Data curation. **Majid Baniassadi:** Writing – review & editing, Supervision, Methodology, Investigation, Formal analysis. **Mahdi Bodaghi:** Writing – review & editing, Validation, Supervision, Methodology, Investigation, Formal analysis, Conceptualization. **Mostafa Baghani:** Writing – review & editing, Supervision, Methodology, Investigation, Formal analysis.

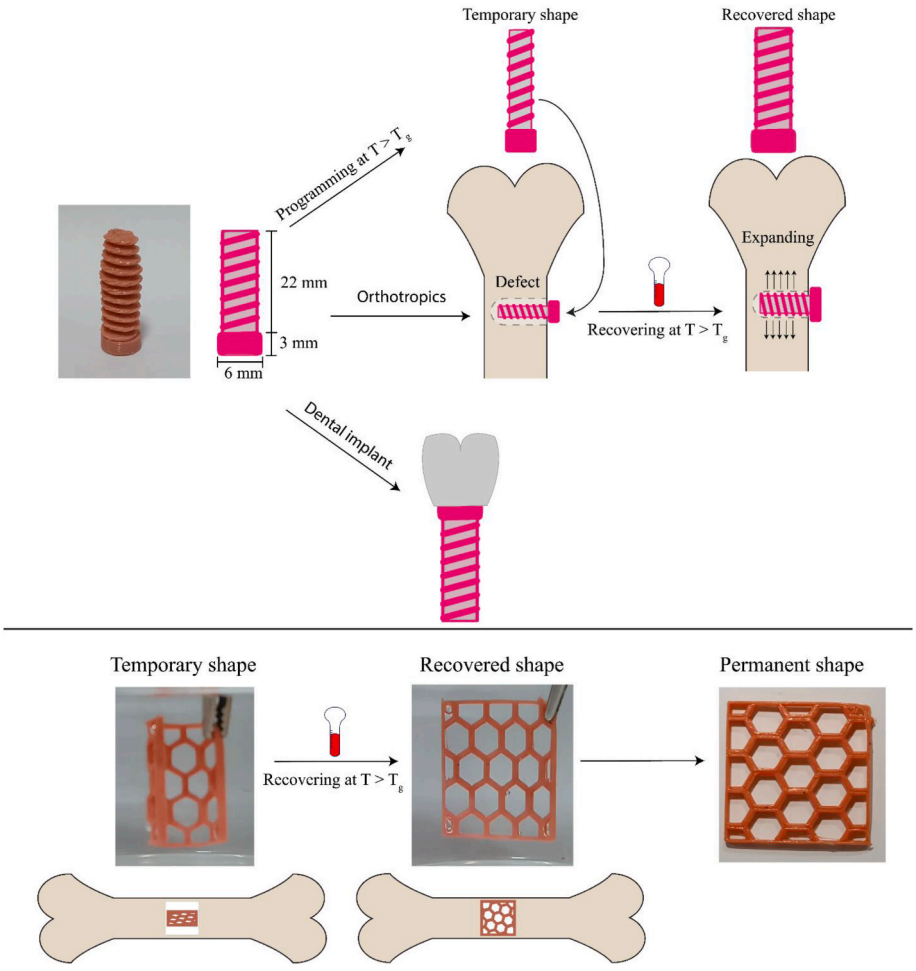

Fig. 13. 3D printed bio-screw and bio-scaffold and their potential application.

Declaration of competing interest

The authors declare that they have no known competing financial interests or personal relationships that could have appeared to influence the work reported in this paper.

Data availability

Data will be made available on request.

Acknowledgment

Mahdi Bodaghi acknowledges the support by the UK Engineering and Physical Sciences Research Council (EPSRC) [Grant No. EP/Y011457/1].

Appendix A. Supplementary data

Supplementary data to this article can be found online at https://doi.org/10.1016/j.jmbbm.2024.106719.

References

Alshebly, Y.S., Nafea, M., Mohamed Ali, M.S., Almurib, H.A.F., 2021. Review on recent advances in 4D printing of shape memory polymers. Eur. Polym. J. 159, 110708 https://doi.org/10.1016/j.eurpolymj.2021.110708.

Anakabe, J., Orue, A., Zaldua Huici, A.M., Eceiza, A., Arbelaiz, A., 2018. Properties of PLA/PMMA blends with high polylactide content prepared by reactive mixing in presence of poly(styrene-co-glycidyl methacrylate) copolymer. J. Appl. Polym. Sci. 135 (43) https://doi.org/10.1002/app.46825.

Asvar, Z., Mirzaei, E., Azarpira, N., Geramizadeh, B., Fadaie, M., 2017. Evaluation of electrospinning parameters on the tensile strength and suture retention strength of polycaprolactone nanofibrous scaffolds through surface response methodology. J. Mech. Behav. Biomed. Mater. 75, 369–378. https://doi.org/10.1016/j.jmbbm.2017.08.004.

Buckley, P.R., McKinley, G.H., Wilson, T.S., Small, W., Benett, W.J., Bearinger, J.P., McElfresh, M.W., Maitland, D.J., 2006. Inductively heated shape memory polymer for the magnetic actuation of medical devices. IEEE Trans. Biomed. Eng. 53 (10), 2075–2083. https://doi.org/10.1109/TBME.2006.877113.

Chen, J., Hu, J., Leung, A.K.L., Chen, C., Zhang, J., Zhang, Y., Zhu, Y., Han, J., 2018. Shape memory ankle–foot orthoses. ACS Appl. Mater. Interfaces 10 (39), 32935–32941. https://doi.org/10.1021/acsami.8b08851.

da Cunha, R.B., Cavalcanti, S.N., Agrawal, P., de Figueiredo Brito, G., de Mélo, T.J.A., 2023. Evaluation of shape memory effect in PLA/copolymers blends. J. Appl. Polym. Sci. 140 (42) https://doi.org/10.1002/app.54561.

Das, R., Karthika, S., Bhasarkar, J., Bal, D.K., 2023. GA-coupled ANN model for predicting porosity in alginate gel scaffolds. J. Mech. Behav. Biomed. Mater. 148, 106204 https://doi.org/10.1016/j.jmbbm.2023.106204.

Dayyoub, T., Maksimkin, A.V., Filippova, O.V., Tcherdyntsev, V.V., Telyshev, D.V., 2022. Shape memory polymers as smart materials: a review. Polymers 14 (17), 3511. https://doi.org/10.3390/polym14173511.

Domingo-Espin, M., Travieso-Rodriguez, J.A., Jerez-Mesa, R., Lluma-Fuentes, J., 2018. Fatigue performance of ABS specimens obtained by fused filament fabrication. Materials 11 (12), 2521. https://doi.org/10.3390/ma11122521.

Donate, R., Monzón, M., Alemán-Domínguez, M.E., 2020. Additive manufacturing of PLA-based scaffolds intended for bone regeneration and strategies to improve their biological properties. E-Polymers 20 (1), 571–599. https://doi.org/10.1515/epoly-2020-0046.

Ertiletskaya, N., Avramchenko, A., Prokopchuk, Y., Shalygina, T., Boyandin, A., Sukhanova, A., 2023. Comparative study of physical and chemical properties of PLA-based films obtained by solution casting and flat-slot die melt extrusion. BIO Web Conf 67, 03015. https://doi.org/10.1051/bioconf/20236703015.

Fang, L., Yan, W., Chen, S., Duan, Q., Herath, M., Epaarachchi, J., Liu, Y., Lu, C., 2023. Light and shape-memory polymers: characterization, preparation, stimulation, and application. Macromol. Mater. Eng. 308 (12) https://doi.org/10.1002/mame.202300158.

Feng, J., Fu, J., Yao, X., He, Y., 2022. Triply periodic minimal surface (TPMS) porous structures: from multi-scale design, precise additive manufacturing to multidisciplinary applications. Int. J. Extrem. Manuf. 4 (2), 022001 https://doi.org/10.1088/2631-7990/ac5be6.

Gastaldi, M., Spiegel, C.A., Vazquez-Martel, C., Barolo, C., Roppolo, I., Blasco, E., 2023. 4D printing of light activated shape memory polymers with organic dyes. Mol Syst Des Eng 8 (3), 323–329. https://doi.org/10.1039/D2ME00201A.

Gaxiola-López, J.C., Lara-Ceniceros, T.E., Silva-Vidaurri, L.G., Advincula, R.C., Bonilla-Cruz, J., 2022. 3D printed parahydrophobic surfaces as multireaction platforms. Langmuir 38 (25), 7740–7749. https://doi.org/10.1021/acs.langmuir.2c00788.

Gregor, A., Filová, E., Novák, M., Kronek, J., Chlup, H., Buzgo, M., Blahnová, V., Lukášová, V., Bartoš, M., Nečas, A., Hošek, J., 2017. Designing of PLA scaffolds for bone tissue replacement fabricated by ordinary commercial 3D printer. J. Biol. Eng. 11 (1), 31. https://doi.org/10.1186/s13036-017-0074-3.

Hassan, R.U., Jo, S., Seok, J., 2018. Fabrication of a functionally graded and magnetically responsive shape memory polymer using a 3 <scp>D</Scp> printing technique and its characterization. J. Appl. Polym. Sci. 135 (11) https://doi.org/10.1002/app.45997.

Hu, G., Bodaghi, M., 2023. Direct fused deposition modeling 4D printing and programming of thermoresponsive shape memory polymers with autonomous 2D-to-3D shape transformations. Adv. Eng. Mater. 25 (19) https://doi.org/10.1002/adem.202300334.

Kiyani, S., Taheri-Behrooz, F., Asadi, A., 2021. Analytical and finite element analysis of shape memory polymer for use in lumbar total disc replacement. J. Mech. Behav. Biomed. Mater. 122, 104689 https://doi.org/10.1016/j.jmbbm.2021.104689.

Lalegani Dezaki, M., Bodaghi, M., 2023. Sustainable 4D printing of magneto-electroactive shape memory polymer composites. Int. J. Adv. Des. Manuf. Technol. 126 (1–2), 35–48. https://doi.org/10.1007/s00170-023-11101-0.

Li, A., Fan, J., Li, G., 2018. Recyclable thermoset shape memory polymers with high stress and energy output *via* facile UV-curing. J Mater Chem A Mater 6 (24), 11479–11487. https://doi.org/10.1039/C8TA02644K.

Luo, L., Zhang, F., Wang, L., Liu, Y., Leng, J., 2024. Recent advances in shape memory polymers: multifunctional materials, multiscale structures, and applications. Adv. Funct. Mater. 34 (14) https://doi.org/10.1002/adfm.202312036.

Mora, P., Schäfer, H., Jubsilp, C., Rimdusit, S., Koschek, K., 2019. Thermosetting shape memory polymers and composites based on polybenzoxazine blends, alloys and copolymers. Chem. Asian J. 14 (23), 4129–4139. https://doi.org/10.1002/asia.201900969.

Moradi, M., Lalegani Dezaki, M., Kheyri, E., Rasouli, S.A., Aghaee Attar, M., Bodaghi, M., 2023. Simultaneous FDM 4D printing and magnetizing of iron-filled polylactic acid polymers. J. Magn. Magn Mater. 568, 170425 https://doi.org/10.1016/j.jmmm.2023.170425.

Naresh, D., Raju, R., Parveen, S., 2024. Design and development of alternate layer printing method to reduce the porosity in FDM printing process. Int. J. Interact. Des. Manuf. 18 (5), 3439–3448. https://doi.org/10.1007/s12008-023-01624-x.

Ni, C., Chen, D., Yin, Y., Wen, X., Chen, X., Yang, C., Chen, G., Sun, Z., Wen, J., Jiao, Y., Wang, C., Wang, N., Kong, X., Deng, S., Shen, Y., Xiao, R., Jin, X., Li, J., Kong, X., Zhao, Q., Xie, T., 2023. Shape memory polymer with programmable recovery onset. Nature 622 (7984), 748–753. https://doi.org/10.1038/s41586-023-06520-8.

Niu, X., Wang, M., Xia, Y., Zhu, Y., Jia, X., Cao, R., Wang, X., 2022. Self-healing, thermadapt triple-shape memory ionomer vitrimer for shape memory triboelectric nanogenerator. ACS Appl. Mater. Interfaces 14 (44), 50101–50111. https://doi.org/10.1021/acsami.2c13294.

Nugroho, W.T., Dong, Y., Pramanik, A., Leng, J., Ramakrishna, S., 2021. Smart polyurethane composites for 3D or 4D printing: general-purpose use, sustainability and shape memory effect. Compos. B Eng. 223, 109104 https://doi.org/10.1016/j.compositesb.2021.109104.

Pathak, J.A., Colby, R.H., Kamath, S.Y., Kumar, S.K., Stadler, R., 1998. Rheology of miscible blends: SAN and PMMA. Macromolecules 31 (25), 8988–8997. https://doi.org/10.1021/ma9805708.

Raja, S., Mustafa, Mohammed Ahmed, Ghadir, Ghadir Kamil, Al-Tmimi, Hayder Musaad, Khalid Alani, Zaid, Ali Rusho, Maher, Rajeswari, N., 2024. Unlocking the potential of polymer 3D printed electronics: challenges and solutions. Applied Chemical Engineering 7 (2), 3877. https://doi.org/10.59429/ace.v7i2.3877.

Rodrigues, N., Benning, M., Ferreira, A.M., Dixon, L., Dalgarno, K., 2016. Manufacture and characterisation of porous PLA scaffolds. Procedia CIRP 49, 33–38. https://doi.org/10.1016/j.procir.2015.07.025.

Saeed, M.U., Hang, G., Hu, J., Gao, Y., Li, L., Zhang, T., Zheng, S., 2024. Nanocomposites of polyhydroxyurethane with Fe $_3$ O $_4$ nanoparticles: synthesis, shape memory and photothermal properties. Polym. Eng. Sci. https://doi.org/10.1002/pen.26845.

Samal, S., Svomova, B., Spasovová, M., Tyc, O., Vokoun, D., Stachiv, I., 2023. Physical, thermal, and mechanical characterization of PMMA foils fabricated by solution casting. Appl. Sci. 13 (2), 1016. https://doi.org/10.3390/app13021016.

Samuel, C., Barrau, S., Lefebvre, J.-M., Raquez, J.-M., Dubois, P., 2014. Designing multiple-shape memory polymers with miscible polymer blends: evidence and origins of a triple-shape memory effect for miscible PLLA/PMMA blends. Macromolecules 47 (19), 6791–6803. https://doi.org/10.1021/ma500846x.

Shanmugam, V., Babu, K., Kannan, G., Mensah, R.A., Samantaray, S.K., Das, O., 2024. The thermal properties of FDM printed polymeric materials: a review. Polym. Degrad. Stabil. 228, 110902 https://doi.org/10.1016/j.polymdegradstab.2024.110902.

Shi, P., Schach, R., Munch, E., Montes, H., Lequeux, F., 2013. Glass transition distribution in miscible polymer blends: from Calorimetry to rheology. Macromolecules 46 (9), 3611–3620. https://doi.org/10.1021/ma400417f.

Shi, Z., Zhao, G., Wang, G., Zhang, L., Wei, C., Chai, J., 2023. Development of ultralight, tough and hydrophobic polymethylmethacrylate/polyvinylidene fluoride shape memory foams for heat insulation applications. Mater. Des. 225, 111527 https://doi.org/10.1016/j.matdes.2022.111527.

Shirzad, M., Zolfagharian, A., Matbouei, A., Bodaghi, M., 2021. Design, evaluation, and optimization of 3D printed truss scaffolds for bone tissue engineering. J. Mech. Behav. Biomed. Mater. 120, 104594 https://doi.org/10.1016/j.jmbbm.2021.104594.

Sondagar, H.D., Kumar, S., Sharma, V.S., 2024. A state-of-the-art review of 4D printing techniques, stimuli activated materials and future perspectives. Mater. Today Proc. https://doi.org/10.1016/j.matpr.2024.01.006.

Spiegel, C.A., Hackner, M., Bothe, V.P., Spatz, J.P., Blasco, E., 2022. 4D printing of shape memory polymers: from macro to micro. Adv. Funct. Mater. 32 (51) https://doi.org/10.1002/adfm.202110580.

Subash, A., Kandasubramanian, B., 2020. 4D printing of shape memory polymers. Eur. Polym. J. 134, 109771 https://doi.org/10.1016/j.eurpolymj.2020.109771.

Tancogne-Dejean, T., Diamantopoulou, M., Gorji, M.B., Bonatti, C., Mohr, D., 2018. 3D plate-lattices: an emerging class of low-density metamaterial exhibiting optimal isotropic stiffness. Adv. Mater. 30 (45), 1803334 https://doi.org/10.1002/adma.201803334.

Xia, Y., He, Y., Zhang, F., Liu, Y., Leng, J., 2021. A review of shape memory polymers and composites: mechanisms, materials, and applications. Adv. Mater. 33 (6) https://doi.org/10.1002/adma.202000713.

Yadav, D., Chhabra, D., Kumar Garg, R., Ahlawat, A., Phogat, A., 2020. Optimization of FDM 3D printing process parameters for multi-material using artificial neural network. Mater. Today Proc. 21, 1583–1591. https://doi.org/10.1016/j.matpr.2019.11.225.

Zhang, J., Luo, S., 2024. A novel pellet-based 3D printing of high stretchable elastomer. Proc Inst Mech Eng B J Eng Manuf. https://doi.org/10.1177/09544054241245468.

Zhang, B., Wang, L., Song, P., Pei, X., Sun, H., Wu, L., Zhou, C., Wang, K., Fan, Y., Zhang, X., 2021. 3D printed bone tissue regenerative PLA/HA scaffolds with comprehensive performance optimizations. Mater. Des. 201, 109490 https://doi.org/10.1016/j.matdes.2021.109490.

Zhao, W., Yue, C., Liu, L., Liu, Y., Leng, J., 2023. Research progress of shape memory polymer and 4D printing in biomedical application. Adv. Healthcare Mater. 12 (16) https://doi.org/10.1002/adhm.202201975.

Zolfagharian, A., Durran, L., Gharaie, S., Rolfe, B., Kaynak, A., Bodaghi, M., 2021. 4D printing soft robots guided by machine learning and finite element models. Sens Actuators A Phys 328, 112774. https://doi.org/10.1016/j.sna.2021.112774.

Zolfagharian, A., Lakhi, M., Ranjbar, S., Sayah Irani, M., Nafea, M., Bodaghi, M., 2023. 4D printing parameters optimisation for Bi-stable soft robotic gripper design. J. Braz. Soc. Mech. Sci. Eng. 45 (4), 224. https://doi.org/10.1007/s40430-023-04171-4.